hep-ph/9412245

MPI-PhT/94-86
December 1994

Production of Heavy Selectrons in $e^-\gamma$ Collisions

Debajyoti Choudhury

debchou@surya11.cern.ch
Theory Division, CERN, CH–1211 Genève 23, Switzerland

Frank Cuypers

cuypers@iws166.mppmu.mpg.de
Max-Planck-Institut für Physik, Werner-Heisenberg-Institut, Föhringer Ring 6, D–80805 München, Germany

Abstract

We study the production and decay of heavy selectrons in the $e^-\gamma$ mode of a linear collider of the next generation. The standard model backgrounds can be substantially reduced by appropriate kinematical cuts. As a consequence, selectrons far heavier than the kinematical threshold for pair production are shown to be easily discoverable for large portions of the supersymmetry parameter space. We also describe a model-independent kinematical measurement of the mass of the lightest neutralino.

1 Introduction

One of the most promising ideas that take us beyond the standard model is supersymmetry [1]. However, while it cures many of the ills that plague the standard model, it has its own attendant problems, not the least of which is the fact that, till date, we have seen no evidence for its existence. This naturally sets a minimum scale for the breaking of this symmetry. A second problem deals with the proliferation of parameters in such a theory, especially in the context of the soft supersymmetry breaking terms that must be introduced. Though several attempts [2] have been made to constrain the parameter space by demanding consistency with the experimentally measured rates for low–energy processes, such bounds are most often easily evaded if the mass splittings between supersymmetric particles of a given kind are comparatively small. In addition, such constraints have the drawback of being of an indirect nature and hence dependent on cancellations (or lack thereof) between the contributions from various diagrams with different virtual exchanges.

A complementary (or even better) method would be to look for an actual production of the superpartners in high energy collisions. Of course, the direct production of new particles is only possible provided the latter are sufficiently light. Typically, a collider facility requires a center of mass energy comfortably in excess of twice the mass of the particles to be discovered to permit their pair-production. Consequently, the tightest bounds on the weakly interacting supersymmetric sector are at present given by the LEP experiments and come close to $m_Z/2$.

In this article, we aim to perform an analysis in the context of the linear colliders which are currently being planned, such as CLIC, JLC, NLC, TESLA, VLEPP, *etc.*. To be specific, we concentrate on the "canonical" design with a center of mass energy $\sqrt{s} = 500$ GeV, an electron beam polarization of 90% and an integrated luminosity of 10 fb^{-1}. Though most often these machines are thought of in terms of e^+e^- facilities, they can also be transformed to function in the e^-e^-, $\gamma\gamma$ and $e^-\gamma$ modes. The last-mentioned is the one which is most suitable for our purpose as it lends itself to single selectron production, circumventing in this way the kinematic bound that pair production entails in e^+e^-, e^-e^- and $\gamma\gamma$ collisions.

The production of a single selectron in association with a neutralino was analyzed in Refs [3,4]. We improve these studies here by taking fully into account the gaugino mixings, considering polarized electron and photon beams and performing a detailed analysis of the differential cross sections of the signal and its standard model backgrounds. The latter allows us to devise very efficient kinematical cuts which dramatically enhance the signal to background ratio. As a result, the supersymmetry parameter space can be explored much

deeper than previously expected [3].

In the next Section we describe the production and decay of a selectron in $e^-\gamma$ scattering, as well as the dominant standard model backgrounds. In Section 3 we explain how photon beams can be obtained at a linear collider. We study in the following Section the kinematical characteristics of the event distributions for the signal and background reactions. Armed with this knowlegde, we analyze in Section 5 which regions of the supersymmetry parameter space can be explored with the machine described above. Finally, we summarize our results in the Conclusion.

2 Signal and Backgrounds

We restrict ourselves to the minimal supersymmetric standard model with unbroken R–parity. In most realistic scenarios, the lightest supersymmetric particle is the lightest neutralino $\tilde{\chi}_1^0$, which is stable and hence escapes detection. We concentrate here on the reaction

$$e^-\gamma \longrightarrow \tilde{e}^-\tilde{\chi}_1^0 \ , \tag{1}$$

and the subsequent selectron decay

$$\tilde{e}^- \longrightarrow e^-\tilde{\chi}_1^0 \ . \tag{2}$$

The branching ratio for this decay can be as high as nearly 100%, but it can also be substantially lower if other two body decay modes are kinematically allowed:

$$\tilde{e}^- \longrightarrow e^-\tilde{\chi}_i^0 \qquad (i = 2,3,4) \ , \tag{3}$$
$$\tilde{e}^- \longrightarrow \nu_e\tilde{\chi}_i^- \qquad (i = 1,2) \ , \tag{4}$$

where the $\tilde{\chi}_i^0$ and $\tilde{\chi}_i^-$ are any of the neutralinos or charginos in the theory.

Obviously both the cross section (1) and the partial decay rate (2) depend on the details of the supersymmetric extension, particularly the masses and the mixing angles in the chargino and neutralino sectors. These receive contributions not only from terms originating in the naive supersymmetrization of the standard model lagrangian, but also from soft supersymmetry breaking terms. The chargino mass matrix, in the $(\tilde{W}^- \ \tilde{h}^-)$ basis is given by [1]

$$M_- = \begin{pmatrix} M_2 & \sqrt{2}M_W c_\beta \\ \sqrt{2}M_W s_\beta & \mu \end{pmatrix} \ , \tag{5}$$

whereas the neutralino mass matrix, in the $(\tilde{\gamma}^0\ \tilde{Z}^0\ \tilde{h}_1^0\ \tilde{h}_2^0)$ basis, is

$$M_0 = \begin{pmatrix} M_1 c_w^2 + M_2 s_w^2 & (M_1 - M_2) c_w s_w & 0 & 0 \\ (M_1 - M_2) c_w s_w & M_1 s_w^2 + M_2 c_w^2 & m_Z s_\beta & -m_Z c_\beta \\ 0 & m_Z s_\beta & 0 & -\mu \\ 0 & -m_Z c_\beta & -\mu & 0 \end{pmatrix} . \tag{6}$$

Here $M_{1,2}$ are the soft $U(1)_Y$ and $SU(2)_L$ supersymmetry breaking masses which parametrize direct gaugino mass terms, whereas μ is the higgsino mixing mass. Furthermore, $s_w = \sqrt{1 - c_w^2} = \sin\theta_w$ and $s_\beta = \sqrt{1 - c_\beta^2} = \sin\theta_\beta$ where θ_w is the weak mixing angle and $\tan\beta = v_1/v_2$ is the ratio of the vacuum expectation values of the two Higgs fields. We assume the GUT relation

$$M_1 = \frac{5}{3} M_2 \tan^2\theta_w \ , \tag{7}$$

thus leaving us with three parameters namely $\mu, M_2, \tan\beta$. The exact eigensystem has been computed in Ref. [5]. We confirm these results and use them in our calculations.

One further question remains unsettled, though. It concerns possible mixings between the various charged lepton states. However, both constraints from low energy experiments [6] and theoretical studies [7] suggest that such mixings are very small. We shall thus assume these to be absent. Also, for simplicity, we regard $\tilde{e}_L^-$ and $\tilde{e}_R^-$ to be degenerate, with mass $m_{\tilde{e}}$.

The signal we focus on is thus a final state comprising just a single electron associated with missing energy and momentum:

$$e^-\gamma \longrightarrow \tilde{e}^-\tilde{\chi}_1^0 \longrightarrow e^-\tilde{\chi}_1^0\tilde{\chi}_1^0 \ . \tag{8}$$

A considerable background exists, though, on account of the standard model resonant processes

$$e^-\gamma \longrightarrow e^- Z^0 \longrightarrow e^-\nu_i\bar{\nu}_i \tag{9}$$

and

$$e^-\gamma \longrightarrow W^-\nu_e \longrightarrow e^-\nu_e\bar{\nu}_e \ . \tag{10}$$

We neglect non-resonant processes which also contribute to the same observable signature

$$e^- + \gamma \longrightarrow e^- + \nu_i + \bar{\nu}_i \ . \tag{11}$$

where i is a generation index. This is an excellent approximation [8] which provides a clear picture of the kinematic distribution of the final state. We can safely use the narrow width approximation to compute the total and differential cross sections of the processes (8,9), since the decaying particle is either a scalar or it decays invisibly. The subprocess cross sections for these reactions have been first calculated by Renard [9]. They were also calculated for particular helicity combinations in Ref. [10]. The expressions in Ref. [4] carry some minor errors.

For the process (10), though, the spin-angle correlations have to be taken carefully into account, because the final state electron originates from the decay of a *vector* boson. To do this, we have treated this reaction as a resonant $2 \to 3$ process. The analytic expressions for the differential cross sections are too long to be displayed here.

Before embarking on further calculations, it is worth noting that the background process (10) can of course be very simply reduced with polarized electron beams. Unless stated otherwise, we shall consider in the following a 90% right-polarized electron beam.

3 Photon Beams

High energy photon beams can be obtained by back-scattering a laser ray off a high energy electron beam [11]. The result of this Compton scattering is that the electrons are deflected and dumped while the photons are boosted into a hard collimated beam. If the laser is sufficiently intense, all electrons have a chance to interact, so that there is no loss in luminosity.

Consider laser photons of energy E_l ($\mathcal{O}(1)$ eV) and circular polarization P_l scattering with electrons of energy E_b ($\mathcal{O}(10^{11})$ eV) and longitudinal polarization P_b. (In the next sections we will also need to define the polarization P_e of the the other electron beam, which is not Compton-converted.) If the angle between the laser and electron beams be θ_{bl}, the scattering may be parametrized in terms of

$$z = \frac{4E_bE_l}{m_e^2}\cos^2\frac{\theta_{bl}}{2}\ , \tag{12}$$

where m_e is the mass of the electron. For large z, multiple scattering (*e.g.* , pair creation in conjunction with a laser photon) becomes important [12] and this results in a depletion of the high energy end of the spectrum. To prevent

this, one needs to ensure that

$$z \leq 2(1+\sqrt{2}) \ . \tag{13}$$

In the following we shall assume the equality in the above expression. The resultant photon normalized energy spectrum $n(x)$ and polarization $P_\gamma(x)$ are depicted in Figs 1 as functions of the fraction $x = E_\gamma/E_b$ of the electron energy carried by the photon. The underlying analytic expressions are [11]

$$\frac{\mathrm{d}n(x)}{\mathrm{d}x} = \frac{1}{\mathcal{N}} \left\{ 1 - x + \frac{1}{1-x} - \frac{4x}{z(1-x)} + \frac{4x^2}{z^2(1-x)^2} + P_b P_l \frac{x(2-x)}{1-x} \left[\frac{2x}{z(1-x)} - 1 \right] \right\} , \tag{14}$$

$$P_\gamma(x) = \frac{P_l \zeta (2 - 2x + x^2) + P_b x (1+\zeta^2)}{(1-x)(2-2x+x^2) - 4x(z - zx - x)/z^2 - P_b P_l \zeta x (2-x)} \ , \tag{15}$$

where

$$0 \leq x \leq \frac{z}{z+1} \ , \tag{16}$$

$$\mathcal{N} = \frac{z^3 + 18z^2 + 24z + 8}{2z(z+1)^2} + \left(1 - \frac{4}{z} - \frac{8}{z^2}\right) \ln(1+z) + P_b P_l \left[2 - \frac{z^2}{(z+1)^2} - \left(1 + \frac{2}{z}\right) \ln(1+z) \right] \ , \tag{17}$$

$$\zeta = 1 - x(1 + 1/z) \ . \tag{18}$$

By design, the energy of the photons can never reach the beam energy since their spectrum is limited by Eq. (13,16). Furthermore, in practice the low energy tail of the photon spectrum cannot participate in any reaction either. Indeed, as is displayed in the last of Figs 1, there is a one to one relationship between the energy of the back-scattered photons and their angle with respect to the direction of the initial electron: harder photons are emitted at smaller angles whereas softer photons are emitted at larger angles. For small deflection angles from the beam direction we have

$$\theta_\gamma(x) \simeq \frac{m_e}{E_b} \sqrt{\frac{z}{x} - z - 1} \tag{19}$$

Clearly, the photons will be distributed according to an effective spectrum, which effectively throws out the low energy photons, these being produced at too wide an angle to contribute significantly to any reaction. The exact profile of this effective spectrum depends somewhat on the shape of the electron beam. In the absence of a detailed (and machine specific) study of this effect, we approximate this effect by a sharp cut. The position of this cut depends of course crucially on the conversion distance, *i.e.* the distance between the interaction point and the point where the laser photons are back-scattered. For example, if we assume a conversion distance of 5 cm and an interaction spot of 500 nm diameter, then photons scattered at more than 5 μrd are lost. The lowest energy photons would then have $x_{\min} \approx .4$, as can be read from the last of Figs 1. In the following we use (*cf.* Eq. (13))

$$x_{\min} = .5 \qquad x_{\max} = \frac{2+2\sqrt{2}}{3+2\sqrt{2}} \approx 0.8284 \; . \tag{20}$$

We have checked that our final results are not very sensitive to the choice of the first of these two machine parameters. Any cross section is obtained by convoluting the fixed energy scattering cross section with the photon spectrum (14):

$$\mathrm{d}\sigma(s) = \int_{x_{\min}}^{x_{\max}} \mathrm{d}x \; \frac{\mathrm{d}n}{\mathrm{d}x} \, \mathrm{d}\sigma(xs) \; \theta\left(x - \frac{1}{s}\left(\sum_i m_i\right)^2 \right) \; , \tag{21}$$

where the sum runs over the masses of the final state particles.

4 Kinematical Cuts

In the absence of linear polarization, the final state electrons in either the signal or the background processes are characterized by only two independent kinematical variables, say the cosine of their polar angle ($\cos\theta_e$) and their energy (E_e). As it turns out, the distribution of events in this plane is very different for the three processes (8–10). We now proceed to study the boundaries of these distributions in order of increasing complexity.

4.1 $e^-\gamma \to e^- Z^0$

Were the initial state photons monochromatic ($E_\gamma = \sqrt{s}/2$), the final state electrons would be distributed in the $(\cos\theta_e, E_e)$ plane along the line of constant energy $E_e = (s - m_Z^2)/2\sqrt{s}$. Since the energy of the initial state photon

is actually spread between $x_{\min}\sqrt{s}/2 \leq E_\gamma \leq x_{\max}\sqrt{s}/2$ (20), the final state electrons are distributed in phase space region

$$\cos\theta_e = \frac{(1+x)\sqrt{s}E_e - xs + m_Z^2}{(1-x)\sqrt{s}E_e} \qquad x_{\min} \leq x \leq x_{\max} \ . \tag{22}$$

The two boundary curves are displayed in Figs 2 and 3. They confine all the Z^0 events, and will be used as kinematical cuts in the subsequent numerical analysis to entirely eliminate the Z^0 background (9).

4.2 $e^-\gamma \to \tilde{e}^-\tilde{\chi}_1^0 \to e^-\tilde{\chi}_1^0\tilde{\chi}_1^0$

The electrons emerging from the decay of the selectron are distributed within the phase space region

$$E_e = \frac{m_{\tilde{e}}^2 - m_{\tilde{\chi}}^2}{2\left[E_{\tilde{e}} - k_{\tilde{e}}\cos\left(\theta_{\tilde{e}} - \theta_e\right)\right]} \ , \tag{23}$$

where $k_{\tilde{e}} = \sqrt{E_{\tilde{e}}^2 - m_{\tilde{e}}^2}$ is the momentum of the selectrons, whose energy spreads within the region

$$\cos\theta_{\tilde{e}} = \frac{(1+x)\sqrt{s}E_{\tilde{e}} - xs - m_{\tilde{e}}^2 + m_{\tilde{\chi}}^2}{(1-x)\sqrt{s}k_{\tilde{e}}} \qquad x_{\min} \leq x \leq x_{\max} \ . \tag{24}$$

Since the (heavy) selectrons are produced rather isotropically [3], the cosine on the left hand side of Eq. (24) can take any value between -1 and 1. As a consequence, the highest energy of the selectrons is given by

$$E_{\tilde{e}}^{\max} = \frac{1}{4x_{\max}\sqrt{s}}\left[\left(1+x_{\max}\right)\left(x_{\max}s + m_{\tilde{e}}^2 - m_{\tilde{\chi}}^2\right) + \left(1-x_{\max}\right)\sqrt{\left(x_{\max}s + m_{\tilde{e}}^2 - m_{\tilde{\chi}}^2\right)^2 - 4x_{\max}sm_{\tilde{e}}^2}\right] \tag{25}$$

and the energy of the decay electrons is confined within

$$\frac{m_{\tilde{e}}^2 - m_{\tilde{\chi}}^2}{2\left(E_{\tilde{e}}^{\max} + k_{\tilde{e}}^{\max}\right)} \leq E_e \leq \frac{m_{\tilde{e}}^2 - m_{\tilde{\chi}}^2}{2\left(E_{\tilde{e}}^{\max} - k_{\tilde{e}}^{\max}\right)} \ . \tag{26}$$

The two boundary lines are displayed in Figs 2 and 3 for a selectron of mass $m_{\tilde{e}} = 250$ GeV and the particular set of supersymmetry parameters $\mu = 500$ GeV, $M_2 = 400$ GeV and $\tan\beta = 4$. For this choice, the mass of the lightest

neutralino is $m_{\tilde{\chi}_1^0} = 193$ GeV. The available phase space is thus small because the sum of the produced masses $m_{\tilde{e}} + m_{\tilde{\chi}_1^0} = 443$ GeV is so close to the available center of mass energy $\sqrt{x_{\max} s} = 455$ GeV.

Note that the values of the two energy boundaries (26) depend solely on the center of mass energy, the mass of the selectron and the mass of the neutralino. Therefore, a measurement of these two limiting energies provides a direct kinematical determination of the mass of the neutralino. A similar model independent measurement of the neutralino mass can otherwise be performed only in a polarized e^-e^- experiment, if the selectron is light enough to be pair-produced [13].

4.3 $e^-\gamma \to W^-\nu_e \to e^-\bar{\nu}_e\nu_e$

Here the situation is more subtle. At first glance one might expect the decay electrons of the W^- to be subjected to similar kinematical bounds as the decay electrons of the selectrons. Indeed, proceeding with the replacements $m_{\tilde{e}} \leftrightarrow m_W$ and $m_{\tilde{\chi}} \leftrightarrow m_\nu = 0$ in Eqs (23,26), the energy of the W^- decay electrons is in principle only bound by

$$\frac{m_W^2}{2\sqrt{s}} \leq E_e \leq \frac{\sqrt{s}}{2} \ . \tag{27}$$

This range covers almost the entire phase space. However, some improvement can be achieved by identifying the dense regions in phase space. Since the W^- production cross section is very much peaked backwards with respect to the initial electron beam [3], it is a good approximation to set $\cos\theta_W = -1$ in Eqs (23,24). Hence, the most probable energy of the W^- is

$$E_W = \frac{x^2 s + m_W^2}{2x\sqrt{s}} \qquad x_{\min} \leq x \leq x_{\max} \ , \tag{28}$$

and the bulk of the electrons is produced within the phase space region

$$E_e \leq \frac{m_W^2}{2\left(E_W + k_W \cos\theta_e\right)} \ . \tag{29}$$

Since the W^- production cross section increases monotonically with the center of mass energy [3,14], more events occur for larger values of x. In Figs 2 and 3, we have thus displayed the curve corresponding to $x = x_{\max}$ in Eqs (28,29). Clearly, a large portion of the W^- events is confined below this curve. It will therefore be used as a kinematical cut alongwith Eq. (22) in the subsequent numerical analysis.

It should be borne in mind that events which do not satisfy this bound are also kinematically allowed. However, the corresponding rate is strongly suppressd by the dynamics of the W^- production mechanism. One effect of the dynamics can be seen by comparing the density of events plotted on Figs 2 and 3. The only difference consists of different initial state polarizations. Although the choice of Fig 3 confines the W^- events better within the bounds (28,29), far fewer selectrons are produced and the signal to background ratio is worse. This is why we concentrate in the next section on the choice of polarizations used in Fig 2.

5 Results

In addition to the kinematical cuts (22,29) discussed above and depicted in Figs 2 and 3, the signal to background ratio can be further enhanced by dividing the $(\cos\theta_e, E_e)$ phase space into N bins (of equal size, here). The number of events in each bin is then compared with the standard model expectation. This procedure takes automatically into account the information contained in Eq. (26). The significance of the deviation is given by the χ^2 test

$$\chi^2 = \sum_i^N \left(\frac{n^{\rm exp} - n^{\rm SM}}{\Delta n^{\rm exp}} \right)^2 \ , \tag{30}$$

where $n^{\rm SM}$ is the number of events expected for the standard model, $n^{\rm exp} = n(\mu, M_2, \tan\beta, m_{\tilde{e}})$ is the corresponding observed number of events (if supersymmetry is to explain the deviation) and the error Δn is the quadratic combination of statistical and systematic errors on the observed number of events

$$\Delta n = \sqrt{n + (\epsilon n)^2} \ . \tag{31}$$

The relative systematic error ϵ is essentially due to the luminosity measurement (the uncertainty on the electrons' energies and angles is negligible) and is set to 1% in the following.

Clearly, if less than five events are contained in a bin, the probabilistic interpretation of the χ^2 test becomes unreliable. Indeed, with so few events the underlying Poisson distribution does not resemble enough a gaussian shape to warrant the sum (30) to be distributed according to a χ^2. For this reason, we ignore alltogether any bin with less than five events.

Instead of attempting to explore at one go the four-dimensional parameter space *viz.* $(\mu, M_2, \tan\beta, m_{\tilde{e}})$, we choose to present our results in the form of 2-dimensional χ^2 contour plots in the (μ, M_2) plane for different values of $m_{\tilde{e}}$

and $\tan\beta$. We also exhibit the dependence on the polarization of the electron beams P_b and P_e, and on the number of bins N. To obtain the explorable regions at the 95% confidence level we set $\chi^2 = 6$ in Eq. (30).

Unless stated otherwise we use in the following

$$m_{\tilde{e}} = 250 \text{ GeV} \qquad \tan\beta = 4 \ , \tag{32}$$

$$P_l = -1 \equiv 100\% \text{ left} \quad P_b = .9 \equiv 90\% \text{ right} \quad P_e = .9 \equiv 90\% \text{ right} \ , \tag{33}$$

$$N = 3 \times 3 \ . \tag{34}$$

Since we consider a machine operating with a e^+e^- center of mass energy $\sqrt{s}_{\max} = 500$ GeV, selectrons with a mass up to 250 GeV can in principle be pair-produced and detected in the e^+e^- or e^-e^- colliding modes. We therefore display in Fig. 4 observability contours for $m_{\tilde{e}} \geq 250$ GeV, *i.e. beyond the kinematical limit of the parent collider*. As expected, the explorable area shrinks with increasing selectron mass. The sharp drop for small μ can easily be understood as for such values, the lightest supersymmetric particle is primarily a higgsino and (almost) does not couple to the electron. This part of the parameter space can be better explored using the e^+e^- mode to observe chargino pair-production. The regions of parameter space located between the dotted lines are those which could be explored this way at the same collider (or have already been clearly excluded by the LEP experiments) assuming charginos can be observed up to the very threshold for their pair-production. If this limit can indeed be reached in practice, the $e^-\gamma$ mode has a chance of *discovering* supersymmetry where the e^+e^- mode cannot, only if the selectron mass is comprised within $250 < m_{\tilde{e}} < 325$ GeV, and this in a marginal portion of the supersymmetry parameter space. Still, even if supersymmetry has been discovered before, for a 500 GeV machine, the $e^-\gamma$ collider operating mode is the only one susceptible of discovering a selectron heavier than 250 GeV. Even a selectron as heavy as 400 GeV can be observed and studied.

In Fig. 5 we display the $\tan\beta$ dependence. As is easily evinced, the contours tend to become more symmetric for progressively larger values of $\tan\beta$. The reason can be understood by examining the characteristic equation of the matrix (6). In the limit where $\tan\beta = \infty$ there remains only a μ^2 dependence. Similarly, for $|\mu| \gg m_Z$ the dependence on $\tan\beta$ should vanish. This fact is indeed reflected by the convergence of the contours for large values of $|\mu|$.

Some portion of the W background (10) being irreducible, it is important to reduce it as much as possible by polarizing the initial electron beam. As can be inferred from Fig. 6 the incidence of a poor polarization is particularly dramatic in the region $50\,\text{GeV} \lesssim \mu \lesssim 200\,\text{GeV}$, where the supersymmetric signal (8) is small on account of the lightest supersymmetric particle being primarily

a higgsino. Nevertheless, improving the polarization beyond 90% only yields marginal improvements. This is because even though the background is further decreased, the signal remains at the limit of observability. The erratic features of the curve at 95% polarization reflect our rejection of bins containing less than five events.

Finally, in Fig. 7 we turn to the dependence of our results on the binning, more specifically on the number of bins. Since coarser binning loses information about the differential distribution, the improvement in the bounds with better energy and angular resolution is not unexpected [1]. It should be noted, though, that increasing the number of bins results only in a modest increase in sensitivity. This is a direct consequence of the efficient kinematic cuts Eqs (22,29).

The variation of this improvement with μ can again be traced to the neutralino mass matrix (6). For small $|\mu|$, the lightest neutralino has a large higgsino component. As a result, its coupling to the electron and hence both the production cross section (eqn. 1) and the partial decay width (eqn. 2) are suppressed. This leads to a comparatively smaller signal to noise ratio. To offset this loss, additional information as obtained from binning is useful. For large values of $|\mu|$ though, the higgsinos tend to decouple and the lightest neutralino is primarily a gaugino. The signal to background ratio on imposition of the kinematic cuts (22,29) is sufficiently large to render binning almost inconsequential.

6 Conclusions

We have studied the production and decay of heavy selectrons at a linear collider of the next generation operated in its $e^-\gamma$ mode in the context of the minimal supersymmetric standard model. While the other modes (e^+e^-, e^-e^- and $\gamma\gamma$) are limited by the kinematical limit of $m_{\tilde{e}} < \sqrt{s}/2 = 250$ GeV, the $e^-\gamma$ option can discover selectrons which are much heavier, up to 400 GeV. The standard model background can be controlled by a judicious choice of beam polarizations and kinematical cuts.

The phase space distribution of the signal final state electrons stands out significantly from the background. This allows to infer in a model-independent way the mass of the selectron as well as that of the invisible lightest neutralino, the lightest supersymmetric particle.

[1] This improvement is not a monotonic function of bin cardinality, as very fine binning would leave too few events in each, thus disqualifying them from contributing to the χ^2 function. As a matter of fact, a 4×4 binning already degrades the resolution!

References

[1] H.P. Nilles, *Phys. Rep.* **110** (1984) 1;
H.E. Haber and G.L. Kane, *Phys. Rep.* **117** (1985) 75.

[2] J. Ellis and D.V. Nanopoulos, *Phys. Lett.* **B110** (1982) 44;
R. Barbieri and R. Gatto, *Phys. Lett.* **B110** (1982) 211;
M. Duncan, *Nucl. Phys.* **B221** (1983) 285;
J. Donoghue, H.-P. Nilles, and D. Wyler, *Phys. Lett.* **B128** (1983) 55;
A. Bouquet, J. Kaplan and C.A. Savoy, *Phys. Lett.* **B148** (1984) 69;
F. Gabbiani and A. Masiero, *Nucl. Phys.* **B322** (1989) 235;
S. Bertolini, F. Borzumati, A. Masiero and G. Ridolfi, *Nucl. Phys.* **B353** (1991) 591;
J. Hagelin, S. Kelley and T. Tanaka, *Nucl. Phys.* **B415** (1994) 293; *Mod. Phys. Lett.* **A8** (1993) 2737.

[3] F. Cuypers, G.J. van Oldenborgh and R. Rückl, *Nucl. Phys.* **B383** (1992) 45 [hep-ph/9205209].

[4] D.L. Borden, D. Bauer and D.O. Caldwell, SLAC preprint SLAC-PUB-5715 (1992).

[5] M. Guchait, *Zeit. für Physik* **C57** (1993) 157; *ibid.* **61** (1994) 178.

[6] D. Choudhury, F. Eberlein, A. König, J. Louis and S. Pokorski, MPI preprint MPI-PhT/94-51 [hep-ph/9408275].

[7] V. Kaplunovsky and J. Louis, *Phys. Lett.* **B306** (1993) 269.

[8] A. Aeppli, F. Cuypers and G.J. van Oldenborgh, *Phys. Lett.* **B314** (1993) 413 [hep-ph/9303236].

[9] F.M. Renard, *Zeit. für Physik* **C14** (1982) 209.

[10] L. Bento and A.M. Mourao, *Zeit. für Physik* **C37** (1988) 587.

[11] I.F. Ginzburg, G.L. Kotkin, V.G. Serbo and V.I. Telnov, *Nucl. Instr. Meth.* **205** (1983) 47.

[12] V.I. Telnov, *Nucl. Instr. Meth.* **294** (1990) 72.

[13] F. Cuypers, G.J. van Oldenborgh and R. Rückl, *Nucl. Phys.* **B409** (1993) 128 [hep-ph/9305287].

[14] I.F. Ginzburg, G.L. Kotkin, S.L. Panfil and V.G. Serbo, *Nucl. Phys.* **B228** (1983) 285.

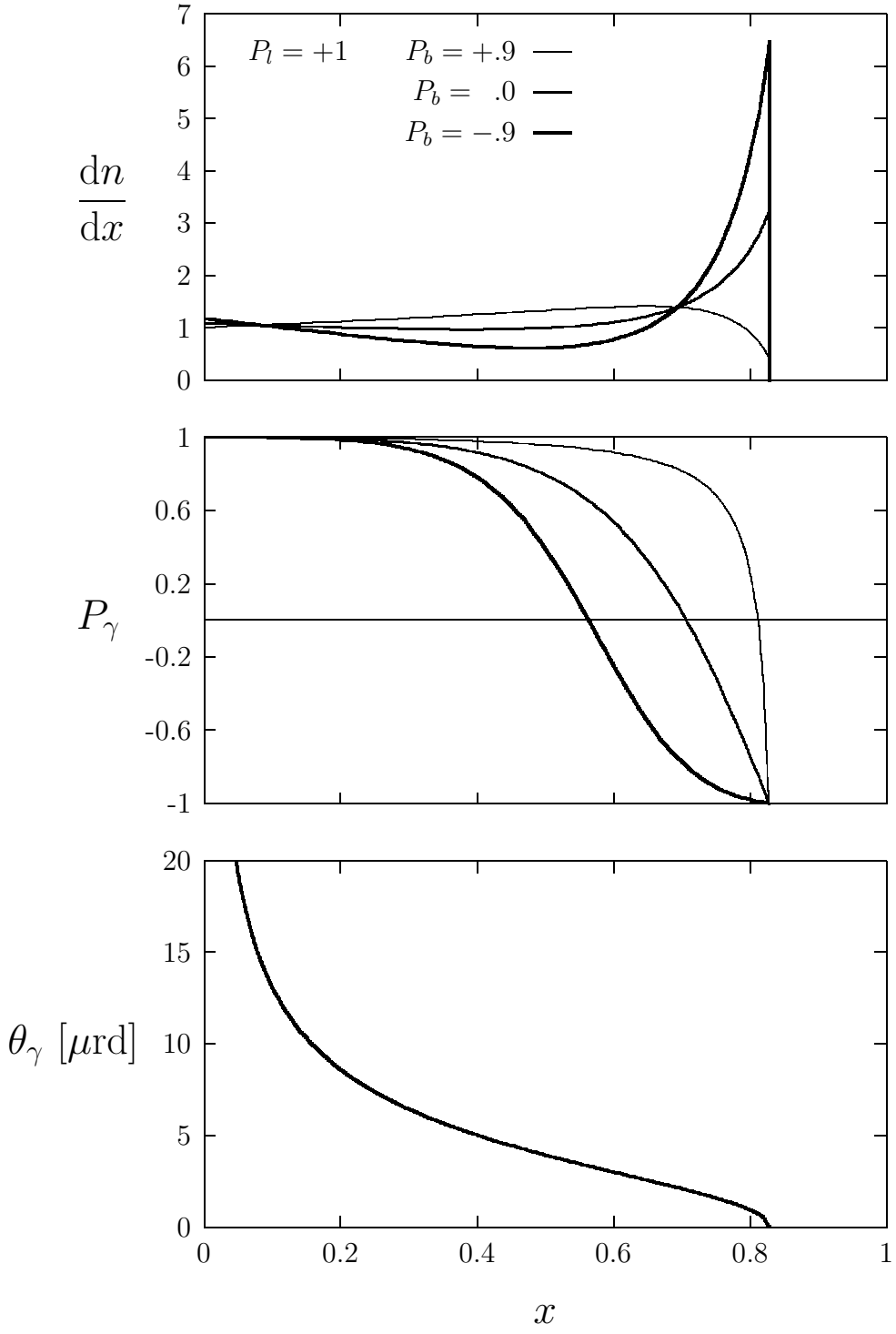

Fig. 1. Back-scattered photon energy spectrum, polarization and polar angle as functions of $x = E_\gamma/E_b$ for three different combinations of beam polarizations.

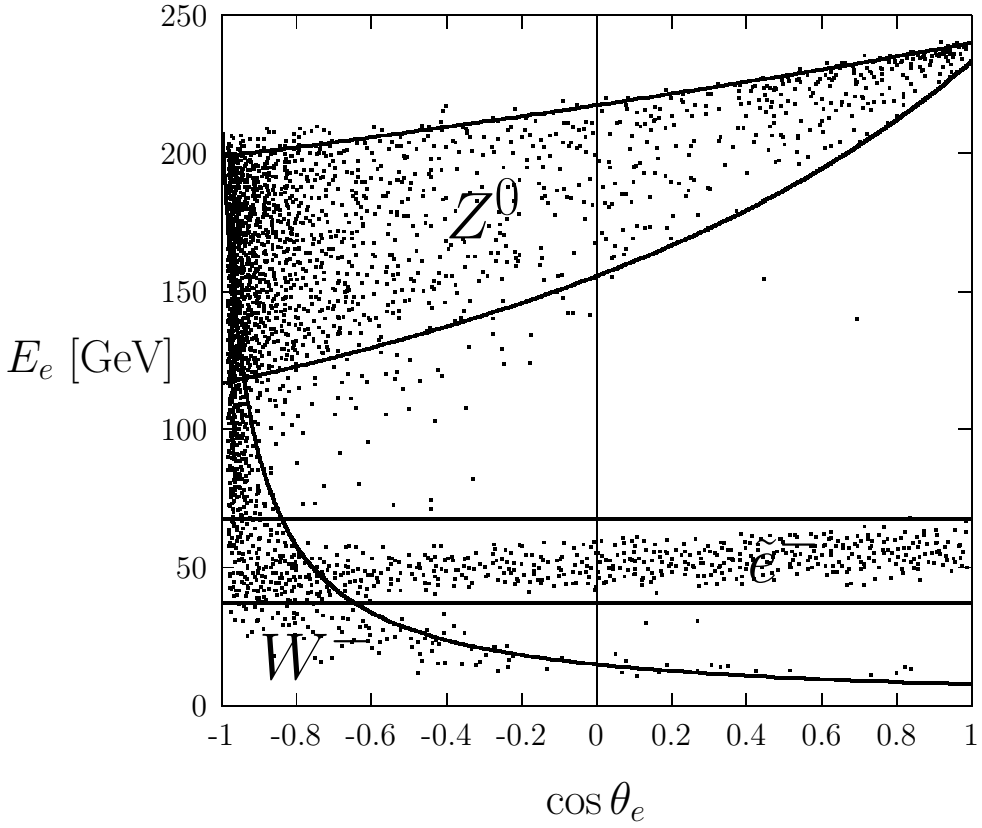

Fig. 2. Scatter plot showing the angle–energy distributions for the final state electrons emanating from the processes (8,9,10). Assuming an integrated luminosity of 10 fb^{-1} each points corresponds to one event. The curves show the exact $(Z^0, \tilde{e}^-)$ or approximate (W^-) kinematically allowed ranges. The laser photons are 100% left polarized whereas both electron beams are 90% right polarized $(P_l = -1 \quad P_b = +.9 \quad P_e = +.9)$.

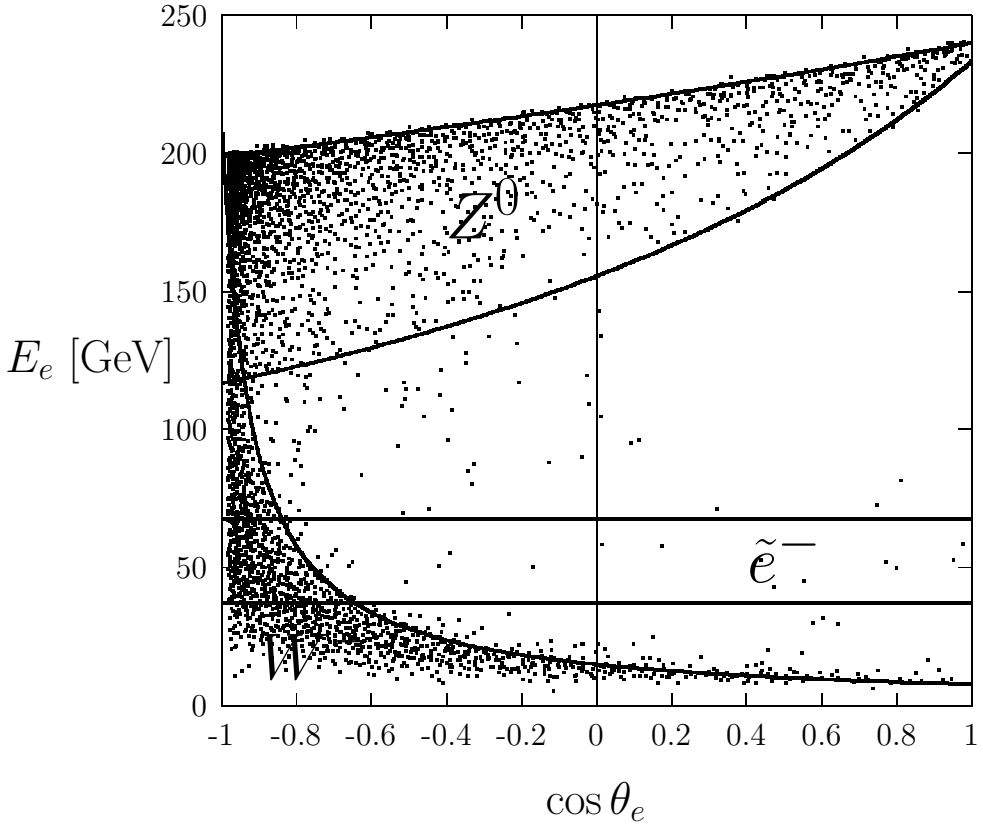

Fig. 3. Same as Fig. 2, except for the laser and Compton-converted electron beams which have now opposite polarizations ($P_l = +1 \quad P_b = -.9 \quad P_e = +.9$).

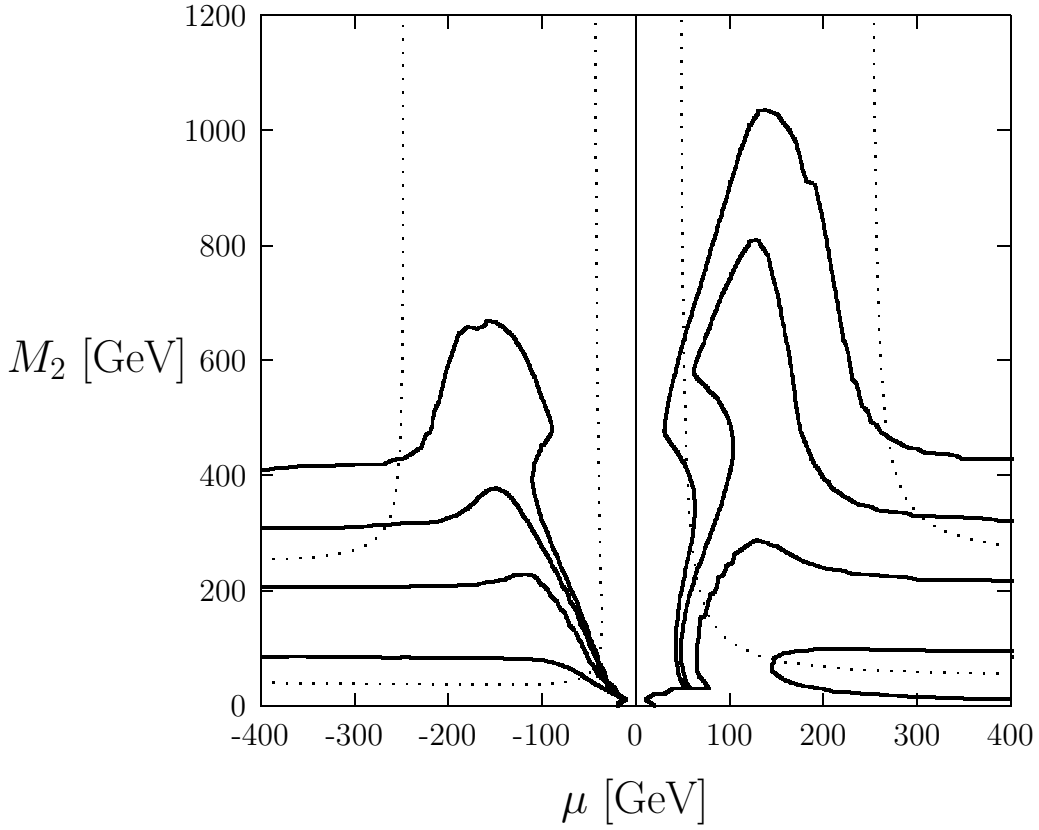

Fig. 4. Contours of $\chi^2 = 6$ for selectron masses $m_{\tilde{e}} = 250, 300, 350, 400$ GeV (from upper to lower curves). All other parameters are specified in Eqs (32–34). The areas below the plain curves can be explored with 95% confidence. The dotted curves delimit the region already excluded by LEP I (lower curves) and the region below which charginos can be pair-produced at the same linear collider run in the e^+e^- mode (upper curves).

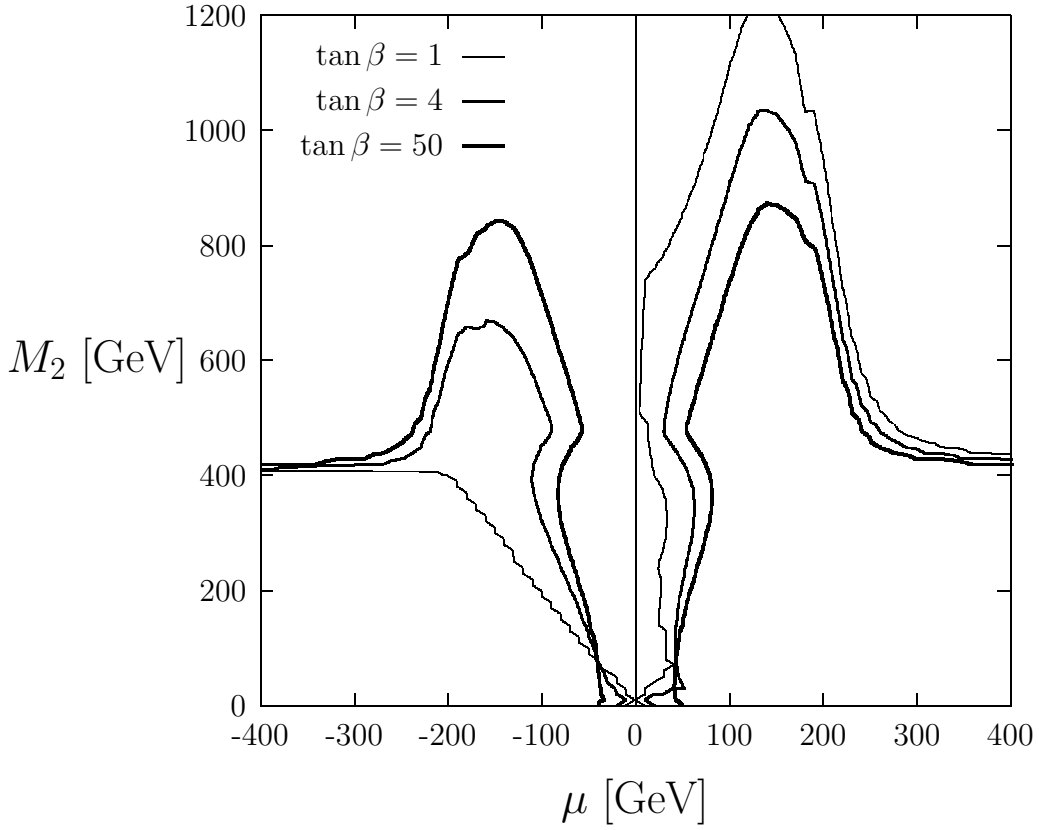

Fig. 5. Contours of $\chi^2 = 6$ for $\tan\beta = 1, 4, 50$. All other parameters are specified in Eqs (32–34). The areas below the curves can be explored with 95% confidence.

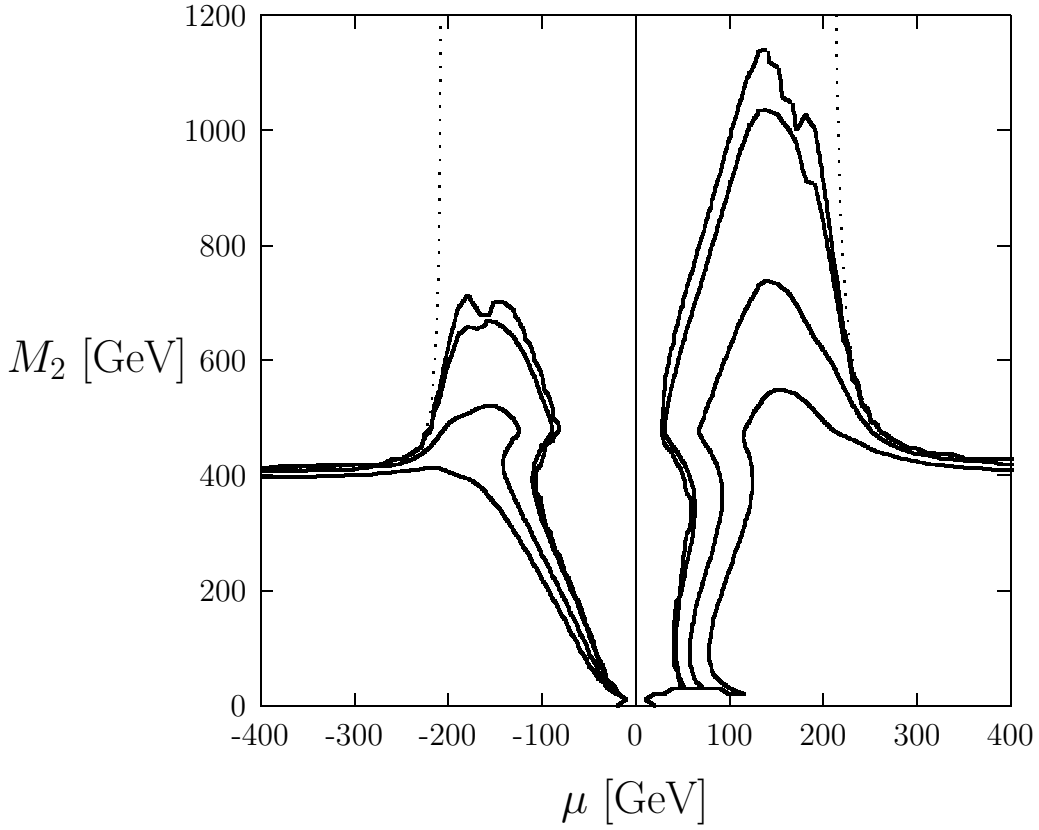

Fig. 6. Contours of $\chi^2 = 6$ for electron beam polarizations $P_b = P_e = 0, 50, 90, 95\%$ (from lower to upper curves). All other parameters are specified in Eqs (32–34). The areas below the curves can be explored with 95% confidence. The dotted curves depict the kinematical limit of the supersymmetric reaction (8).

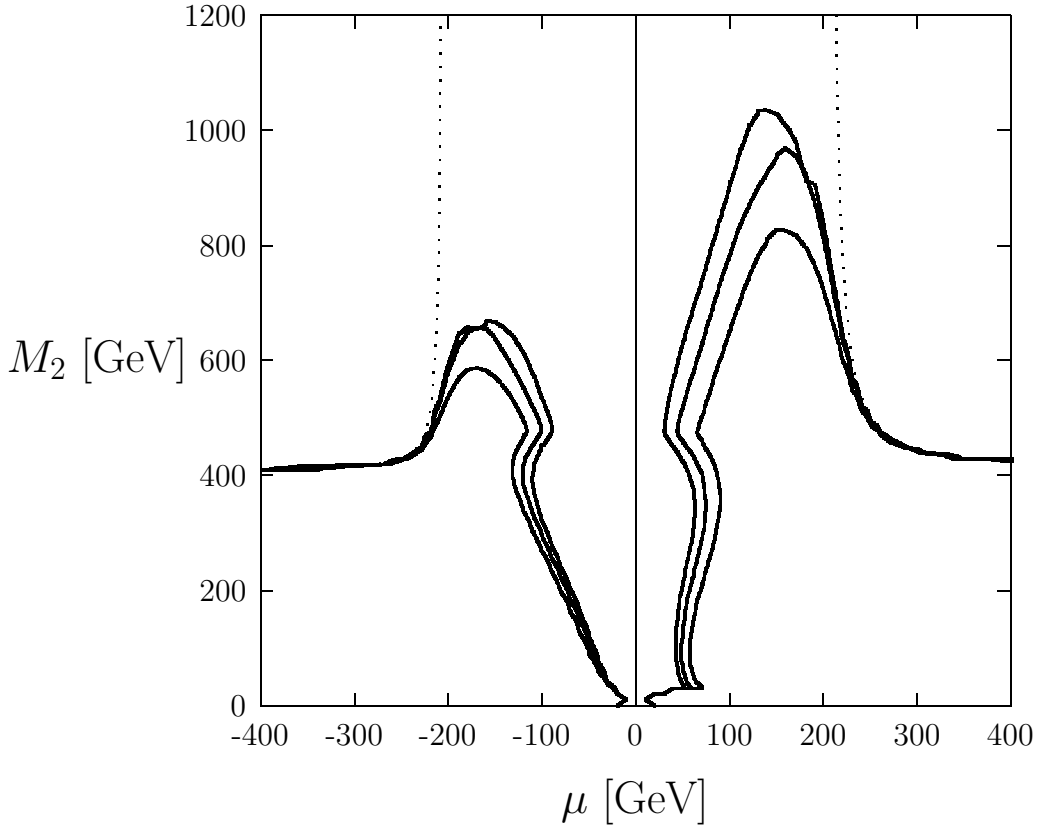

Fig. 7. Contours of $\chi^2 = 6$ for a number of bins $N = 1 \times 1, 2 \times 2, 3 \times 3$ (from lower to upper curves). All other parameters are specified in Eqs (32–34). The areas below the curves can be explored with 95% confidence. The dotted curves depict the kinematical limit of the supersymmetric reaction (8).